Northumbria Research Link

www.northumbria.ac.uk/nrl

northumbria
UNIVERSITY NEWCASTLE

Research Article

Rational design of Pd-TiO$_2$/g-C$_3$N$_4$ heterojunction with enhanced photocatalytic activity through interfacial charge transfer

Tayirjan Taylor Isimjan[1,*], Shahid Rasul[2], Maher Nasser Aloufi[1], Mohd Adnan Khan[1], Ibrahim Khalid Alhowaish[1] and Toseef Ahmed[3]

[1]Fundamental Catalysis, SABIC-CRD at KAUST, *Thuwal*, Saudi Arabia
[2]King Abdullah University of Science and Technology (KAUST), Physical Science and Engineering Division, *Thuwal, 23955–6900*, Saudi Arabia
[3]SABIC Technology Center, *Riyadh*, Saudi Arabia

*Corresponding author. E-mail: isimjant@sabic.com

Abstract

A hybrid heterojunction-based photocatalyst is synthesized by an electrostatic self-assembly strategy including surface modification and controlled metal deposition. The interfacial contact was made by mixing negatively charged anatase TiO$_2$ nanoparticles with positively charged g-C$_3$N$_4$. Visible-light deposition of Pd nanoparticles largely on TiO$_2$ was made possible due to the charge transfer from C$_3$N$_4$ (excited by visible light) to the conduction band of TiO$_2$ reducing Pd ions on contact with its surface. In order to further test the efficiency of this cascade of electron transfer across the conduction bands of the two semiconductors, photocatalytic H$_2$ production from water was studied. Upon optimizing the ratio of the two semiconductors, increased H$_2$ production rates were observed and attributed to enhanced charge separation. Catalysts were studied by a variety of techniques in order to probe into their properties and link them to activity. The reaction rate, under visible-light excitation, of the best sample showed an 8-fold enhancement when compared to that of Pd-C$_3$N$_4$ in identical conditions and the highest apparent quantum yield of 31% was achieved by a 0.1%Pd/20%TiO$_2$/C$_3$N$_4$ sample in a 420- to 443-nm range.

Keywords: surface charge; heterojunction; photocatalyst; electrostatic self-assembly; hydrogen generation

Introduction

While TiO$_2$ is one of the most promising photocatalysts, its application is hindered by its wide band gap energy, corresponding to a negligible fraction of the total solar energy on the Earth. To circumvent this, a good deal of effort has been devoted to developing visible-light-responsive TiO$_2$-based photo catalysts. These types of catalysts can be largely divided into two categories: either TiO$_2$ doped by other elements [1–7] or TiO$_2$ coupled with smaller band gap semiconductors such as C$_3$N$_4$ [8–12], CdS [13, 14], MoS$_2$ [15, 16] and In$_2$S$_3$ [17] as photo-sensitizers. For the second approach, identifying a stable narrow bandgap semiconductor with a suitable band alignment with TiO$_2$ is a challenge. Among these semiconductors, graphitic carbon nitride (g-C$_3$N$_4$) is attractive because its conduction band edge is above that of TiO$_2$ and it possesses excellent chemical stability. Because g-C$_3$N$_4$, itself suffers from rapid charge
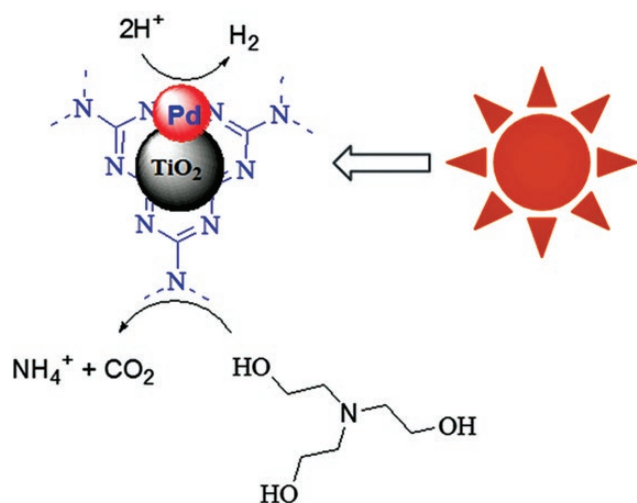
carrier recombination rates, resulting in low photocatalytic activity [18], the quality of the interface with TiO_2 is crucial for the photocatalytic activity of the nanocomposites. For the coupling to be successful, the semiconductors need to fulfil at least the following two requirements: (i) an appropriate band structure that creates a potential offset between the two semiconductors, generating a band bending at the interface, which impels photo-generated electrons and holes to diffuse in opposite directions [19]; and (ii) the crystal structure and orientation of the two semiconductors need to match (at least in part) to minimize point and crystallographic defects [18]. To that end, it has been reported, based on detailed crystallographic studies, that a stable interface can be formed between the (22-40) plane of g-C_3N_4 and the (110) plane of TiO_2(B) (monoclinic, space group C2/m), because both planes have the same d-spacing (0.35 nm) and similar crystal orientation [20].

Overall, the two main strategies used to synthesize g-C_3N_4-TiO_2 nanocomposites are direct mixing or simultaneous synthesis of C_3N_4/TiO_2 nanocomposites. For instance, Peng et al. [21] prepared g-C_3N_4–Pt-TiO_2 (P25) composites by chemical adsorption and reported (at a mass ratio of 70:30 of C_3N_4 to TiO_2) a mild increase in the H_2-generation rate under visible light with stable photocurrent, 1.5 times higher than that of pure g-C_3N_4. Liu et al. reported an *in situ* growth C_3N_4-sensitized TiO_2 nanotube array-based photoanode that gave around a 7-fold improvement in the photocurrent under light irradiation (300–900 nm) when compared to TiO_2 NTs [22]. However, these methods result in self-aggregation, leading to phase separation between TiO_2 and C_3N_4, and they consequently minimize the direct crystal contact between the two semiconductors to form a suitable interface for efficient charge transfer.

As an alternative approach, electrostatic self-assembly is used to construct C_3N_4-based heterojunction structures in which two semiconductors are attached through opposite charges. The nanocomposites synthesized through electrostatic interaction are constructed either by using intrinsic surface charge of the materials [11, 23–27] or by surface functionalization with opposite charges [28–31].

For example, Li et al. [32] fabricated 1D Ag@AgVO$_3$ nanowire/graphene/protonated g-C_3N_4 nanosheet heterojunctions via a simple electrostatic self-assembly process followed by photochemical reduction. The resulting catalyst showed much higher photo-activity on degrading methylene blue compared to that of g-C_3N_4. Similarly, Fan et al. [27] fabricated g-C_3N_4/Zn_2GeO_4 photocatalysts by utilizing opposite electrostatic interaction between two nanoparticles. The heterojunction system showed higher visible-light photocatalytic activity towards the degradation of methylene blue than those of pure g-C_3N_4 and pure Zn_2GeO_4. In addition, Wu et al. reported an electrostatic self-assembly strategy to fabricate a 2D/2D hybrid photocatalyst (g-C_3N_4/rGO) by incorporating reduced graphene oxide (rGO) and protonated g-C_3N_4 in which they used the intrinsic negative charge of rGO and positive surface charge of PCN [33]. Also, Li et al. reported the synthesis of an oxygen reduction (ORR) catalyst prepared by mixing phosphorus-doped graphitic carbon nitride nanosheets with NH_2-functionalized carbon black and they achieved similar performance with a standard ORR catalyst (Pt/Vulcan XC-72) [34].

These results proved that electrostatic interaction-based synthesis is a most efficient way to make nanocomposite because the high zeta potential not only separates similar semiconductor nanoparticles from each, other but also increases the interaction between different semiconductors through opposite-charge repulsion to form a well-dispersed nanocomposite. It not possible to formulate TiO_2/C_3N_4 without surface modification. Nevertheless, there are no reports on electrostatic self-assembling of TiO_2 and g-C_3N_4.

In this work, we have designed, synthesized and tested a Pd-TiO_2/g-C_3N_4 hybrid system through surface-charge interaction wherein both TiO_2 and C_3N_4 exhibited high Z-potentials, therefore preventing self-aggregation while generating enough driving force to form a uniformly mixed heterojunction and then Pd was deposited preferentially on the TiO_2 through visible-light deposition. Finally, a uniformly dispersed Pd-TiO_2/C_3N_4 was synthesized. The high level of uniformity was confirmed by EDX mapping. Moreover, the photocatalytic H_2-generation rate of the best-performing sample 0.1%Pd-20%TiO_2/g-C_3N_4 was found to be 14- and 8-fold higher than that of the prepared g-C_3N_4 and 0.1%Pd/C_3N_4, respectively. In the end, we proposed the related charge-transfer mechanism. We believe this unique two-step approach, including the electrostatic interaction and the directed metal deposition, can be used as a universal method to prepare various heterojunction systems.

1 Experiment

All reagents were of analytical grade, from Sigma-Aldrich and used without further purification. Detailed synthetic procedures are described below.

1.1 Synthesis of Pd-TiO2/g-C3N4

1.1.1 Sulphonic acid-functionalized TiO$_2$ (TiO$_2$-SO$_3$Na)

A typical synthesis is described as follows. (i) To 3 g of TiO$_2$ (anatase) in 30 mL dry ethanol and 1 mL of H$_3$PO$_4$, 3 mL of (3-mercaptopropyl) trimethoxysilane was added and the reaction mixture was refluxed for 24 h. After this period, the mixture was filtered, washed with acetone and dried in air to obtain TiO$_2$-SH. (ii) The resulting TiO$_2$-SH was dispersed in 10 wt.% H$_2$O$_2$ in methanol (20 mL) and stirred for 24 h at room temperature. The prepared sample was then treated with 1 N H$_2$SO$_4$ at ambient temperature for complete protonation, filtered, re-dispersed in water, adjusted pH = 10. The resulting dispersion was filtered and washed with H$_2$O and acetone to obtain TiO$_2$-SO$_3$Na.

1.1.2 Positively charged g-C$_3$N$_4$

The g-C$_3$N$_4$ was prepared from urea at 675°C for 4 h with a heating rate of 0.5 °C/min. The yield was around 6%, consistently with other reported yields [35–37]; 1 g of as-prepared g-C$_3$N$_4$ was added to 200 mL of HCl (1 M) solution and ultra-sonicated for 1 h, stirred for 4 h, centrifuged, washed with DI water and then dried at 80°C for 12 h.

1.1.3 TiO$_2$-SO$_3$(–)/C$_3$N$_4$(+)

Positively charged g-C$_3$N$_4$(+) was dispersed in 70 mL of DI water and then added dropwise to certain amounts of TiO$_2$-SO$_3$Na dispersed in 30 mL of DI water. The resulting mixture was stirred at 25°C overnight, filtered and dried at 80°C for 3 h followed by calcination at 350°C for 4 h.

1.1.4 0.1%Pd-TiO$_2$/g-C$_3$N$_4$

To a 100-mL suspension of TiO$_2$/g-C$_3$N$_4$ was added 0.3 mL Pd (1 mg/mL). The resulting mixture was stirred under visible light (420–650 nm, 43 mW/cm^2) for 4 h. The suspension was filtered, washed with ethanol and dried at 80°C in the air to give the final product.

1.2 Characterization

UV–vis absorbance spectra of the powdered catalysts were collected over the wavelength range of 250–700 nm using a Thermo Fisher Scientific spectrophotometer equipped with praying mantis diffuse reflectance accessory. Absorbance (A) and reflectance (% R) of the samples were measured. The reflectance (% R) data were used to calculate the band gap of the samples using the Tauc plot (Kubelka–Munk function). XRD spectra were recorded using a Bruker D8 Advance X-ray diffractometer. Cu Kα (λ = 1.5406 Å) radiation over the range of 2θ intervals between 20 and 90° with a step size of 0.010° and a step time of 0.2 s/step was used. XPS spectra of the samples were collected using a Thermo Scientific Escalab 250 XI XP spectrometer with Al Kα X-ray source. The X-ray spot size was 650 × 650 μm^2. The charge compensation was carried out using a standard flood gun. Before collecting

XPS data, samples were etched using Ar ions for 5 min at the ion energy of 1000 eV. The data were acquired using the following settings before and after etching: Pass Energy = 20 eV, Energy Step Size = 0.1 eV and Dwell Time = 100 ms. All the peaks were corrected with respect to the binding energy of adventitious C1s peak at 284.5 eV. All peaks were fitted using SMART background option and the Lorentzian/Gaussian ratio of 0.3. TEM analysis of the samples was performed using a TitanG2 80–300 CT from FEI Instruments that was equipped with a field-emission gun. The analysis was conducted by operating the microscope with a beam energy of 300 keV. TEM specimens were prepared by placing a small number of samples on holey carbon-coated copper (Cu) grids with a mesh size of 300. Several low- and high-resolution electron micrographs were acquired from various locations during the analysis. Fast-Fourier transform (FFT) analysis was applied to various regions of the High-resolution TEM (HRTEM) micrographs to investigate the different crystal structures. Scanning electron microscopy/energy-dispersive X-ray spectroscopy (SEM–EDS) analysis was done at 20 kV (Quanta 200, FEI, OR). Zeta-potential measurement was performed on a zeta potential and submicron particle size analyser equipped with delsa nano auto-titrator (Model DelsaNano C, Beckman Coulter). FT-IR spectra were obtained using the Thermo Nicolet 6700 FT-IR spectrometer. Photoluminescence (PL) spectra were measured at room temperature on an A10094 fluorescence spectrometer (Hamamatsu Photonics K. K., Japan) with an excitation wavelength of 320 nm and the suspension concentration was 0.06 mg/mL in deionized water.

1.3 Photocatalytic tests

Photocatalytic reactions were evaluated in a 137-mL-volume Pyrex glass reactor using 25 mg of catalyst and 30 mL of 10 vol.% triethanol amine (TEA) aqueous solution. The slurry was purged with N$_2$ gas to remove any O$_2$ by constant stirring before the reaction. A xenon lamp (Asahi spectra MAX-303) with a total flux of 42.5 mW/cm (of which the UV contribution is ~3 mW/cm) and visible up to 650 nm at a distance of 2 cm was used. Product analyses were performed by gas chromatography equipped with a thermal-conductivity detector connected to a Porapak Q packed column (2 m) at 45°C and N$_2$ was used as a carrier gas. The apparent quantum yields (AQY) were measured under a light intensity of 43 mW/cm^2 (420–650 nm). The illumination area was 10 cm^2.

1.4 Photocurrent measurements

The analysis was conducted in conventional two-electrode cells on a Biologic electrochemical workstation with the Pt as a counter electrode. The studied samples were ground roughly and 20 mg was dispersed in 1.0 mL of DMF. The mixture was ultrasonically treated to obtain a slurry, which

was spin-coated onto pre-treated FTO glass and the working electrode was further dried at 150°C for 2 h. 10% TEA in 1 M NaOH was used as the electrolyte for the photocurrent response measurements.

2 Results and discussion

The surface-charge method used to prepare the TiO_2/g-C_3N_4 hybrid system is illustrated in Scheme 1. The surface of TiO_2 (1) was modified with 3-mercaptopropyl trimethoxysilane (MPTMS) to thiol-functionalized TiO_2 (2) followed by thiol oxidation to sulphonic acid (2), which was deprotonated by NaOH to form sulphonic ions functionalized TiO_2 (3). A negatively charged suspension of (3) was then uniformly mixed by sonication with a positively charged suspension of C_3N_4 (4) to produce the hybrid composite of TiO_2-SO_3(–)/g-C_3N_4(+) (5), which was annealed at 350°C for 3 h in order to remove the surface ligand and form the targeted hybrid system TiO_2/C_3N_4 (6). Finally, Pd cations were light-deposited on (6) to give Pd-TiO_2/g-C_3N_4 (7).

To monitor the charge of the materials, we performed zeta-potential measurements of the protonated C_3N_4(+), the negatively charged TiO_2-SO_3(–) and the heterojunction made of TiO_2-SO_3(–) (20 wt%)/C_3N_4(+). The zeta potential of C_3N_4(+) was found to be equal to +19.6 mV and that of TiO_2-SO_3(–) was equal to –21.3 mV. The potential difference between the two (40.9 mV) is much higher than that reported in the literature [27]. The high zeta potentials prevent self-aggregation of each component in water and generate enough driving force to form a uniformly dispersed suspension. Cancelation of charges was noticed upon the heterojunction formation where the overall Z-potential of the heterojunction system was +2.5 mV. Therefore, a uniformly dispersed TiO_2/C_3N_4 was achieved through this process.

To further investigate the dispersion of both components, scanning electron microscopy–energy-dispersive X-ray spectroscopy (SEM–EDS) was used to conduct the elemental mapping of Pd(0.1 wt%)-TiO_2(20 wt%)/C_3N_4, Fig. 1. It is clear that the Ti atoms (of TiO_2) were well dispersed over the g-C_3N_4 semiconductor.

XRD patterns of the g-C_3N_4 mixed with different mass ratios from 5 wt% to 30 wt% of TiO_2 are presented in Fig. 2a. Most of the characteristic peaks for both components are visible in all studied ratios. The two main characteristic
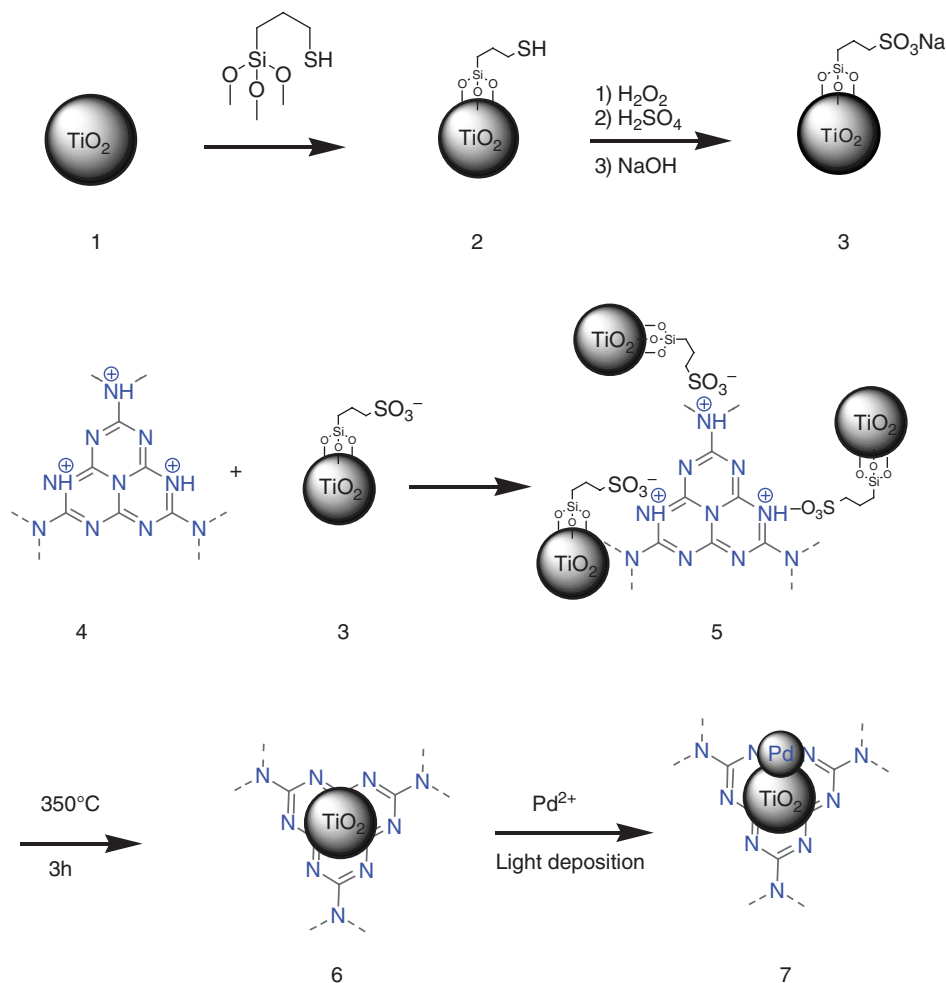
Scheme 1. Schematic diagram for the synthesis of TiO_2/C_3N_4 via chemical modifications and electrostatic self-assembly strategy
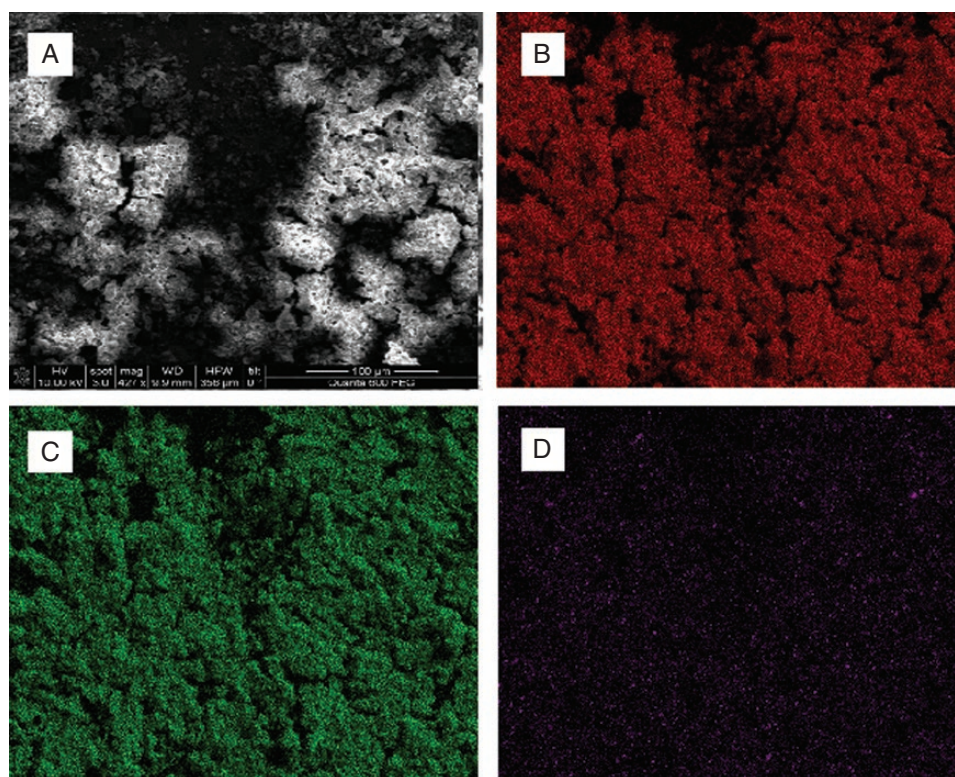
Fig. 1 SEM-EDX mapping areas. (a) Mapping area, (b) carbon, (c) nitrogen and (d) titanium. The scale in Fig. 1a is for 100 μm.

peaks of inter-layer packing (100) and inter-planar stacking (002) of g-C_3N_4 show at 2θ = ~13 and ~27°, respectively, and are observed [38] in addition to the (101) diffraction of the anatase TiO_2 peak. Fig. 2b presents the corresponding diffuse reflectance absorption spectra of the bare 0.1%Pd-g-C_3N_4, TiO_2 and Pd/TiO_2/C_3N_4 series with various TiO_2 and g-C_3N_4 mass ratios. The absorption edge of TiO_2 is not visible from the spectrum. The main absorption edge of g-C_3N_4 occurs around 440 nm and the band gap was estimated to be around 2.8 eV from the Tuac plots (Fig. 2b, insertion).

Morphologies of 0.1% Pd-20% TiO_2/C_3N_4 were investigated by TEM/HRTEM (Fig. 3). Fig. 3a shows that the particle sizes of Pd and TiO_2 are around 5 and 15 nm, respectively. Lattice fringes are shown in Fig. 3c and 3d in which the d-spacing of 0.2 and 0.19 nm correspond to the (200) planes of anatase TiO_2 and Pd, respectively [39]. The corresponding d-spacings from FFT are given in Fig. 3e and f. A further important observation made for Pd/TiO_2/C_3N_4 (Fig. 3b) was the inter-particle heterojunctions between TiO_2 and C_3N_4 as well as TiO_2 and Pd. Although the inter-particle heterojunction between C_3N_4 and Pd was also detected, the Pd density on TiO_2 is much higher than that of C_3N_4, as shown in the STEM (Fig. 3i) and the detailed calculation is shown in Fig. S1 in the online Supplementary Data. Moreover, nanoscale EDXs are performed at the points where TiO_2 and C_3N_4 are separated (Fig. 3g). The Pd signal was only detected on TiO_2 (Fig. 3h). These results clearly indicate that the electron generated by visible light flows from the conduction band of C_3N_4 to that of TiO_2, since the Pd was light-deposited onto the surface of the TiO_2/C_3N_4.

This is also indirect evidence of the proposed mechanism in Fig. 5d.

2.1 XPS spectra of 0.1% Pd-20% TiO_2/g-C_3N_4 (Fig. 4 and Fig. S2 in the online Supplementary Data)

CPS C1, N1s are consistent with those reported for G-C_3N_4 by us [40] and others previously [21, 38, 41–44]. Two points are, however, worth mentioning. First, Pd metal, despite its low loading, was detected (around 0.1 wt%) and similar loading was also measured by ICP (Fig. S3 in the online Supplementary Data): binding energy attributed to Pd $3d_{5/2}$ and $3d_{5/2}$ at 334.4 and 339.4 eV [45]. The presence of S was clear; this was due to the ligand used to link TiO_2 to g-C_3N_4: binding energy at 168 eV attributed to S $2p_{3/2}$ [46] for TiO_2-SO_3Na, indicating that the SH from the previous step was oxidized into –SO_3^- to form negative charges on the TiO_2 surface, supporting Scheme 1.

FT-IR results of the hybrid system are shown in Fig. S4 in the online Supplementary Data, the broadband from 2900 to 3500/cm corresponding to N-H and O-H stretching vibrations; the latter is due to absorbed hydroxyl species [47]. The peaks at 1200–1600/cm correspond to the stretching mode of CN heterocycles as well as the bending modes of adsorbed water and surface hydroxyls [48]. PL measurements were conducted on the best-performing catalyst of 0.1%Pd-20%TiO_2/C_3N_4 (Fig. 5c) and its precursors, in order to probe into the charge-recombination process [49] at room temperature with an excitation wavelength of 320 nm. There is a significant decrease in the PL intensity
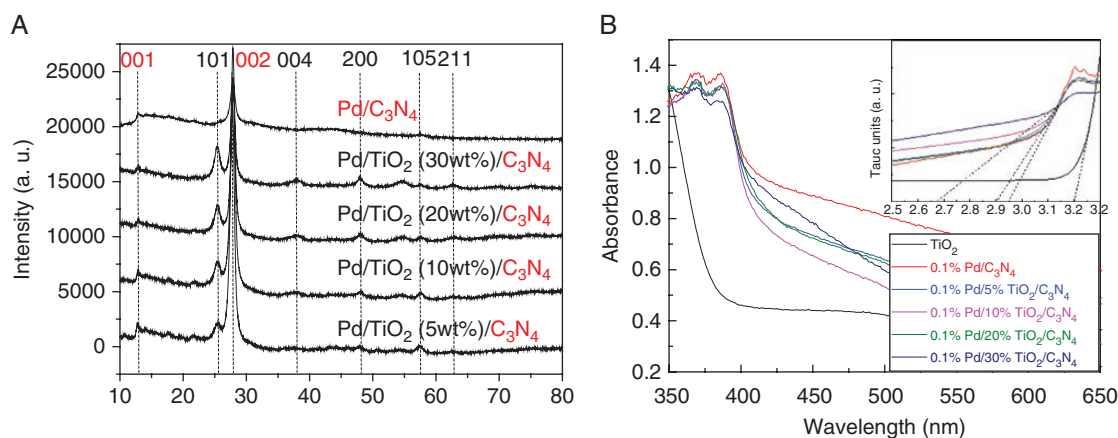
Fig. 2 (a) XRD patterns of 0.1%Pd-g-C_3N_4 and Pd/TiO_2/g-C_3N_4 composites with different mass ratios of TiO_2 and g-C_3N_4. (b) UV–vis diffuse reflectance absorption spectra of the patterns of 0.1%Pd-g-C_3N_4 and Pd-TiO_2/g-C_3N_4 composites with different mass ratios of TiO_2 and g-C_3N_4.
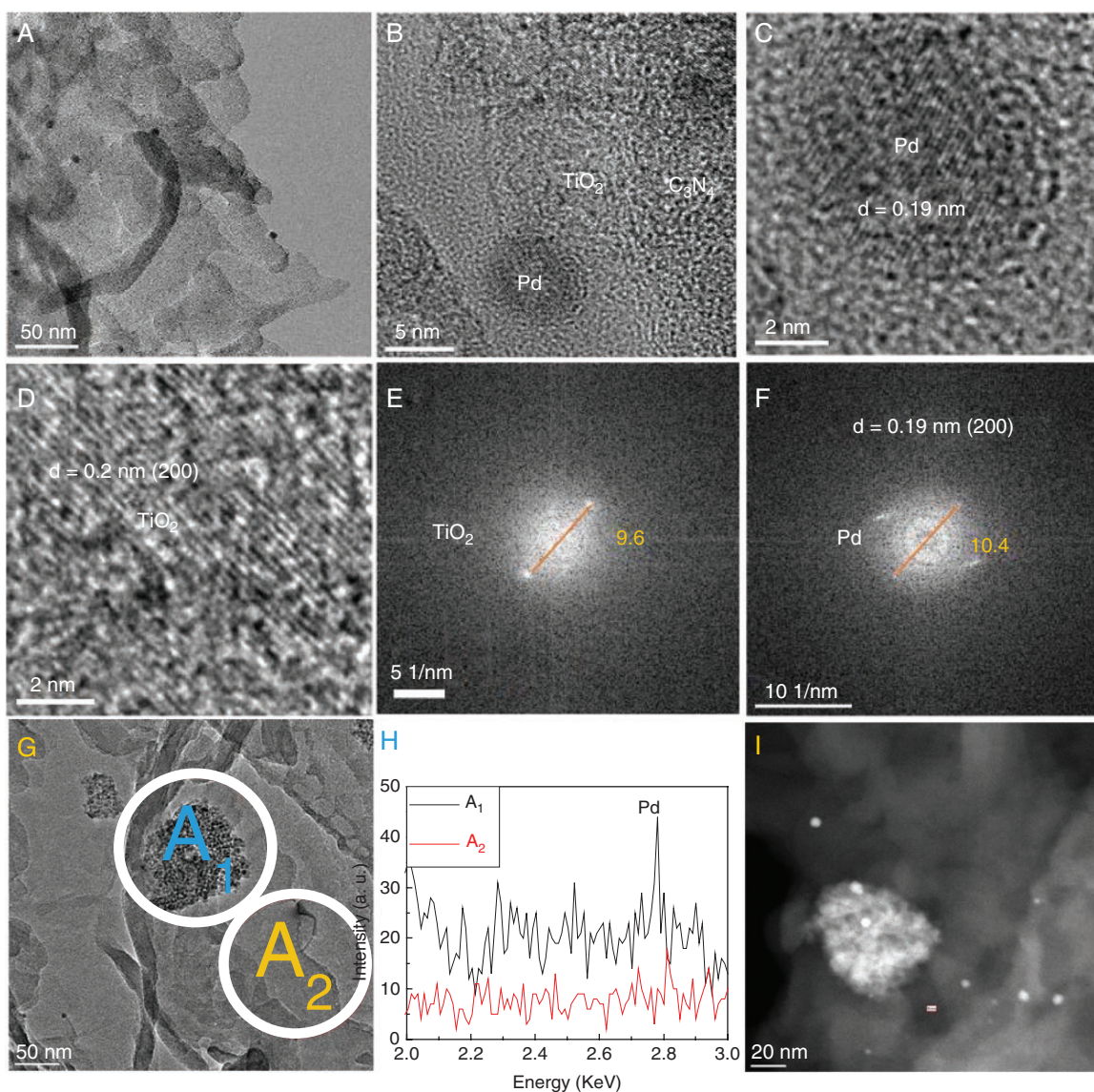
Fig. 3 HR-TEM images of 0.1 wt% Pd/TiO_2/C_3N_4: (a) low magnification, (b) high magnification, (c) lattice fingers of Pd, (d) lattice spacing of TiO_2, (e) FFT diffraction pattern of TiO_2 (d = 0.2nm), (f) FFT diffraction pattern of a Pd particle (d = 0.19 nm), (g) TEM images of the areas (circled in orange) that performed EDX analysis, (h) EDX results of the circled areas in (g) and STEM images.
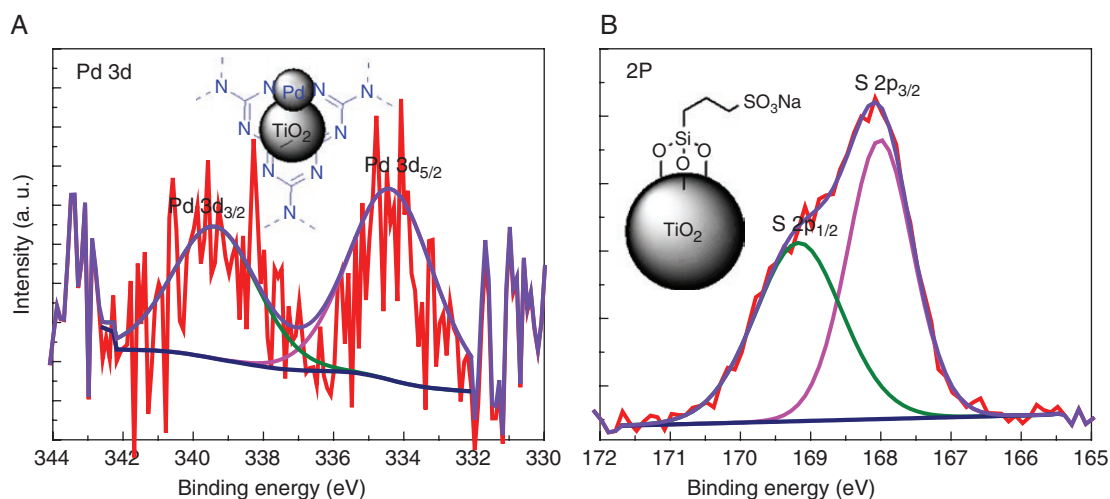
Fig. 4 XPS spectra of 0.1% Pd-TiO$_2$/C$_3$N$_4$ and TiO$_2$-SO$_3$Na. (a) Pd 3d, (b) S 2p of TiO$_2$-SO$_3$Na.

of 0.1% Pd-20%TiO$_2$/C$_3$N$_4$ compared to those of 20%TiO$_2$/C$_3$N$_4$ and pristine g-C$_3$N$_4$. The weak intensity of the PL signal can be attributed to a lower recombination rate of the photo-generated charge carriers [50–52], which is also consistent with other studies over metal-supported TiO$_2$ [53]. Therefore, one can draw the conclusion that introducing TiO$_2$ onto the surface of g-C$_3$N$_4$ could effectively decrease the electron–hole recombination rates. The addition of Pd, even in such a small amount, has resulted in further decreasing the PL signal, which is again further evidence of electron transfer from the conduction band (CB) of the hybrid semiconductor to Pd metal.

The photocatalytic H$_2$ production rates over the Pd-TiO$_2$/g-C$_3$N$_4$ composites containing different mass ratios are shown in Fig. 5a and Fig. S5 in the online Supplementary Data. No H$_2$ production is seen in the absence of either a photocatalyst or light irradiation. Moreover, H$_2$ rates of as-prepared g-C$_3$N$_4$ were very low; it doubled for 0.1% Pd-gC$_3$N$_4$. Because TiO$_2$ anatase has a band gap of about 390 nm, it is not active under visible-light excitation and was not tested. H$_2$ production rates increased considerably for Pd/ x%TiO$_2$/g-C$_3$N$_4$ hybrid catalysts with a maximum observed at ~20% in the investigated range, corresponding the maximum AQY of 31% (420–443 nm), whereas further increasing the content of TiO$_2$ in the composite leads to decrease the H$_2$ production rate. The H$_2$ production rate enhancement along with the increase in TiO$_2$ may be due to the synergistic effect between TiO$_2$ and g-C$_3$N$_4$. The synergic effect could be caused by the electron transfer from HUMO of g-C$_3$N$_4$ to the CB of TiO$_2$ owing to the band positions as shown in Fig. 5d, resulting in a slow charge recombination [21]. Moreover, Pd as an H$_2$ co-catalyst and meanwhile acting as an electron drain hinders the charge recombination; therefore, the H$_2$-generation rate was further improved. On the other hand, the decrease in photo-activity upon increasing the TiO$_2$ mass ratio may be attributed to the fact that there are not enough active sides of g-C$_3$N$_4$ to be exposed for

photo-oxidation because of the excess surface coverage by TiO$_2$. Furthermore, the excess TiO$_2$ may cause aggregation of TiO$_2$ nanoparticles that also creates the bulk resistance for electron transfer. Interestingly, the H$_2$-generation rate of Pd/TiO$_2$/g-C$_3$N$_4$ is extremely low—almost at zero under UV and UV–vis, which means the electron–hole recombination was enhanced on the interface when both semiconductors were activated at the same time. Others also observed the same phenomena [21]. The stability test was conducted on the best-performing catalyst for up to 20 h and almost no degradation was detected (Fig. S6 in the online Supplementary Data).

A fast and steady photocurrent response was observed for each working electrode (Fig. 5b). The highest photocurrent density was achieved on Pd/ TiO$_2$(20 wt%)/g-C$_3$N$_4$, which is more than 10 times that of Pd/C$_3$N$_4$ and the great enhancement in the photocurrent can be ascribed to the improved charge separation and accelerated change transfer by the selective positioning of Pd on TiO$_2$.

The reported value of the band positions of the highest occupied molecular orbital and the lowest unoccupied molecular orbital (LUMO) of C$_3$N$_4$ are –1.3 and 1.4 eV, respectively [54]. The CB and valence band band edge potentials of anatase TiO$_2$ are reported as –0.5 and 2.7 eV correspondingly [55]. The proposed charge-transfer mechanism is shown in Fig. 5d. Where, the electron–hole pairs are generated by g-C$_3$N$_4$ under visible-light illumination, the excited electrons migrate to Pd nanoparticles through the CB of TiO$_2$ and are then quenched by 2H$^+$ to form H$_2$ molecules. Subsequently, a better electron–hole separation can be achieved through these multiple electron-transfer processes. Accordingly, the hole that was kept on LUMO of g-C$_3$N$_4$ will be quenched eventually by TEOA [56]. Furthermore, Fig. S8 in the online Supplementary Data shows a schematic diagram of the work function of Pd as well as the band configurations of TiO$_2$ [57] and g-C$_3$N$_4$ [58, 59] before and after contact. As shown in Fig. 8S in the online Supplementary Data, the electrons from the CB of g-C$_3$N$_4$ flow to the Pd through the
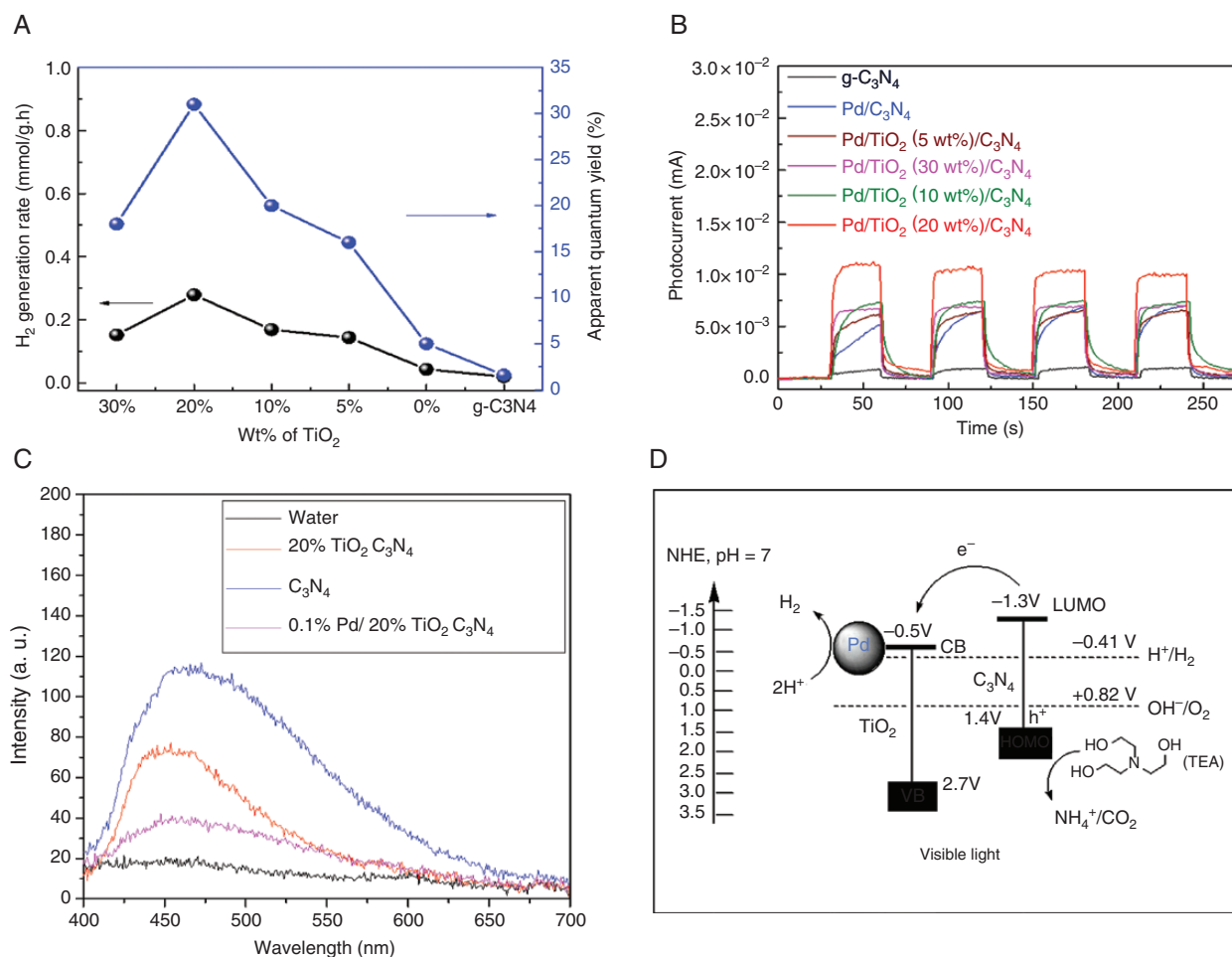
Fig. 5 (a) Photocatalytic H_2 evolution rates of g-C_3N_4, 0.1wt%Pd-g-C_3N_4 and 0.1wt%Pd/TiO_2/g-C_3N_4 composites with different TiO_2/C_3N_4 mass ratios. 20 mg catalyst, 30 mL 10 vol% TAE aqueous solution and 300 W Xe lamp with 23% intensity (43 mW/cm²) for the visible-light ($\lambda \geq 420$ nm) irradiation and the apparent quantum yield (AQY) (420–650 nm, (b) photocurrent responses of the catalysts under Xe lamp irradiation with 400-nm cut-off filter, (c) photoluminescence of pristine g-C_3N_4, 20%TiO_2/C_3N_4 and 0.1% Pd/20%TiO_2/C_3N_4 and (d) proposed charge-transfer mechanism between g-C_3N_4 and TiO_2 through the heterojunction interface under visible-light irradiation.

CB of TiO_2 when the TiO_2 and g-C_3N_4 acquire an equalized Fermi level with the work function of Pd [57]. Furthermore, Pd/TiO_2/g-C_3N_4 nanocomposite inhibits the electron–hole pair recombination ensuing from the enhanced photocatalytic activities of the nanocomposite.

3 Conclusions

In summary, we designed a novel approach to preparing a Pd/TiO_2/g-C_3N_4 hybrid system via four-step processing such as surface modification, mixing, calcination and light-assisted deposition. The synergistic effect of TiO_2 and g-C_3N_4 promoted photo-generated charge separation. Moreover, the Pd was preferentially deposited on the TiO_2 of TiO_2/g-C_3N_4 through light deposition, which remarkably improved the charge transfer between TiO_2 and g-C_3N_4, hindered electron–hole recombination and enhanced the photocatalytic H_2-generation rate. The results show that the photocatalytic H_2-generation rate of optimized sample 0.1%Pd/20% TiO_2/g-C_3N_4 is 14 and 8 times higher than

that of as-prepared g-C_3N_4 and 0.1%Pd/C_3N_4. Most importantly, this work focused on introducing a novel approach using electrostatic interaction and light deposition to fabricate a model nanocomposite of Pd/TiO_2/C_3N_4. In addition, the photocatalytic activities of the Pd/TiO_2/C_3N_4 were measured to further evaluate this approach. The results show that this two-step method is a better way of making nanocomposites. This study provides a novel way of preparing new, stable and visible-light-responsive photocatalysts.

Acknowledgements

Supplementary data

Supplementary data is available at *Clean Energy* online.

References

[1] Hu Z, Xu T, Fang B. Photocatalytic degradation of vehicle exhaust using Fe-doped TiO_2 loaded on activated carbon. *Appl Surf Sci* 2017; 420:34–42.

[2] Zhang Y, Gu D, Zhu L, et al. Highly ordered Fe_{3+}/TiO_2 nanotube arrays for efficient photocataltyic degradation of nitrobenzene. *Appl Surf Sci* 2017; 420:896–904.

[3] Isimjan TT, Trifkovic M, Abdullahi I, et al. Nanoscale optimization and statistical modeling of photoelectrochemical water splitting efficiency of N-doped TiO_2 nanotubes. *Top Catal* 2015; 58:114–22.

[4] Tuichai W, Danwittayakul S, Chanlek N, et al. Effects of sintering temperature on microstructure and giant dielectric properties of (V + Ta) co-doped TiO_2 ceramics. *J Alloys Compd* 2017; 725:310–7.

[5] Isimjan TT, Ruby AE, Rohani S, et al. The fabrication of highly ordered and visible-light-responsive Fe-C-N-codoped TiO_2 nanotubes. *Nanotechnology* 2010; 21:055706.

[6] Szatmáry L, Bakardjieva S, Šubrt J, et al. Sulphur doped nanoparticles of TiO_2. *Catal Today* 2011; 161:23–8.

[7] Wang W, Wang Z, Liu J, et al. Single-step one-pot synthesis of TiO_2 nanosheets doped with sulfur on reduced graphene oxide with enhanced photocatalytic activity. *Scientific Reports* 2017; 7:46610.

[8] Highfield J. Advances and recent trends in heterogeneous photo(electro)-catalysis for solar fuels and chemicals. *Molecules* 2015; 20:6739–93.

[9] Jiang Z, Jiang D, Yan Z, et al. A new visible light active multifunctional ternary composite based on TiO_2-In_2O_3 nanocrystals heterojunction decorated porous graphitic carbon nitride for photocatalytic treatment of hazardous pollutant and H_2 evolution. *Appl Catal B* 2015; 170–171:195–205.

[10] Jiang Z, Liu D, Jiang D, et al. Bamboo leaf-assisted formation of carbon/nitrogen co-doped anatase TiO_2 modified with silver and graphitic carbon nitride: Novel and green synthesis and cooperative photocatalytic activity. *Dalton Trans* 2014; 43:13792–802.

[11] Yang M, Liu J, Zhang X, et al. C_3N_4-sensitized TiO_2 nanotube arrays with enhanced visible-light photoelectrochemical performance. *Phys Chem Chem Phys* 2015; 17:17887–93.

[12] Zang Y, Li L, Xu Y, et al. Hybridization of brookite TiO_2 with g-C_3N_4: a visible-light-driven photocatalyst for As_{3+} oxidation, MO degradation and water splitting for hydrogen evolution. *J Mater Chem A* 2014; 2:15774–80.

[13] Shin K, Park JH. Highly transparent dual-sensitized titanium dioxide nanotube arrays for spontaneous solar water splitting tandem configuration. *ACS Appl Mater Interfaces* 2015; 7:18429–34.

[14] Li J, Cushing SK, Zheng P, et al. Solar hydrogen generation by a CdS-Au-TiO_2 sandwich nanorod array enhanced with au nanoparticle as electron relay and plasmonic photosensitizer. *J Am Chem Soc* 2014; 136:8438–49.

[15] Meng C, Liu Z, Zhang T, et al. Layered MoS_2 nanoparticles on TiO_2 nanotubes by a photocatalytic strategy for use as high-performance electrocatalysts in hydrogen evolution reactions. *Green Chem* 2015; 17:2764–8.

[16] Zhang P, Tachikawa T, Fujitsuka M, et al. Efficient charge separation on 3D architectures of TiO_2 mesocrystals packed with a chemically exfoliated MoS_2 shell in synergetic hydrogen evolution. *Chem Commun* 2015; 51:7187–90.

[17] Chai B, Peng T, Zeng P, et al. Synthesis of floriated In_2S_3 decorated with TiO_2 nanoparticles for efficient photocatalytic hydrogen production under visible light. *J Mater Chem* 2011; 21:14587–93.

[18] Zhao Z, Sun Y, Dong F. Graphitic carbon nitride based nanocomposites: a review. *Nanoscale* 2015; 7:15–37.

[19] Shim M, McDaniel H, Oh N. Prospects for strained type-II nanorod heterostructures. *J Phys Chem Lett* 2011; 2:2722–7.

[20] Zhang L, Jing D, She X, et al. Heterojunctions in g-C_3N_4/TiO_2(B) nanofibres with exposed plane and enhanced visible-light photoactivity. *J Mater Chem A* 2014; 2:2071–8.

[21] Chai B, Peng T, Mao J, et al. Graphitic carbon nitride (g-C_3N_4)-Pt-TiO_2 nanocomposite as an efficient photocatalyst for hydrogen production under visible light irradiation. *Phys Chem Chem Phys* 2012; 14:16745–52.

[22] Yang M, Liu J, Zhang X, et al. C_3N_4-sensitized TiO_2 nanotube arrays with enhanced visible-light photoelectrochemical performance. *Phys Chem Chem Phys* 2015; 17:17887–93.

[23] Hu S, Zhang W, Bai J, et al. Construction of a 2D/2D g-C_3N_4/rGO hybrid heterojunction catalyst with outstanding charge separation ability and nitrogen photofixation performance via a surface protonation process. *RSC Adv* 2016; 6:25695–702.

[24] Hsu YY, Suen NT, Chang CC, et al. Heterojunction of Zinc Blende/Wurtzite in $Zn_{1-x}Cd_xS$ solid solution for efficient solar hydrogen generation: X-ray absorption/diffraction approaches. *ACS Appl Mater Interfaces* 2015; 7:22558–69.

[25] Pu C, Wan J, Liu E, et al. Two-dimensional porous architecture of protonated GCN and reduced graphene oxide via electrostatic self-assembly strategy for high photocatalytic hydrogen evolution under visible light. *Appl Surf Sci* 2017; 399(Supplement C):139–50.

[26] Cheng E, Yin W, Bai S, et al. Synthesis of vis/NIR-driven hybrid photocatalysts by electrostatic assembly of $NaYF_4$:Yb, Tm nanocrystals on g-C3N4 nanosheets. *Mater Lett* 2015; 146(Supplement C):87–90.

[27] Sun L, Qi Y, Jia C-J, et al. Enhanced visible-light photocatalytic activity of g-C_3N_4/Zn_2GeO_4 heterojunctions with effective interfaces based on band match. *Nanoscale* 2014; 6:2649–59.

[28] Qiu Y, Xin L, Jia F, et al. Three-dimensional phosphorus-doped graphitic-C_3N_4 self-assembly with NH_2-functionalized carbon composite materials for enhanced oxygen reduction reaction. *Langmuir* 2016; 32:12569–78.

[29] Jian X, Liu X, Yang HM, et al. Construction of carbon quantum dots/proton-functionalized graphitic carbon nitride nanocomposite via electrostatic self-assembly strategy and its application. *Appl Surf Sci* 2016; 370:514–21.

[30] Dang X, Zhang X, Chen Y, et al. Preparation of β-$Bi_2O_3/g-C_3N_4$ nanosheet p–n junction for enhanced photocatalytic ability under visible light illumination. *J Nanoparticle Res* 2015; 17:1–8.

[31] Liu CG, Wu XT, Li XF, et al. Synthesis of graphene-like g-C_3N_4/Fe_3O_4 nanocomposites with high photocatalytic activity and applications in drug delivery. *RSC Adv* 2014; 4:62492–8.

[32] Zhang S, Li J, Wang X, et al. Rationally designed 1D Ag@AgVO3 nanowire/graphene/protonated g-C_3N_4 nanosheet heterojunctions for enhanced photocatalysis via electrostatic self-assembly and photochemical reduction methods. *J Mater Chem A* 2015; 3:10119–26.

[33] Hu S, Zhang W, Bai J, et al. Construction of a 2D/2D g-C_3N_4/rGO hybrid heterojunction catalyst with outstanding charge separation ability and nitrogen photofixation performance via a surface protonation process. *RSC Adv* 2016; 6:25695–702.

[34] Qiu Y, Xin L, Jia F, et al. Three-dimensional phosphorus-doped graphitic-C_3N_4 self-assembly with NH_2-functionalized carbon composite materials for enhanced oxygen reduction reaction. *Langmuir* 2016; 32:12569–78.

[35] Liu J, Wang H, Antonietti M. Graphitic carbon nitride 'reloaded': emerging applications beyond (photo)catalysis. *Chem Soc Rev* 2016; 45:2308–26.

[36] Mamba G, Mishra AK. Graphitic carbon nitride (g-C3N4) nano-composites: a new and exciting generation of visible light driven photocatalysts for environmental pollution remediation. *Appl Catal B* 2016; 198:347–77.

[37] Ong WJ, Tan LL, Ng YH, et al. Graphitic carbon nitride (g-C$_3$N$_4$)-based photocatalysts for artificial photosynthesis and environmental remediation: are we a step closer to achieving sustainability? *Chem Rev* 2016; 116:7159–329.

[38] Liu J, Zhang T, Wang Z, et al. Simple pyrolysis of urea into graphitic carbon nitride with recyclable adsorption and photocatalytic activity. *J Mater Chem* 2011; 21:14398–401.

[39] Chu L, Qin Z, Yang J, et al. Anatase TiO$_2$ nanoparticles with exposed {001} facets for efficient dye-sensitized solar cells. *Sci Rep* 2015; 5:12143.

[40] Caux M, Fina F, Irvine JTS, et al. Impact of the annealing temperature on Pt/g-C$_3$N$_4$ structure, activity and selectivity between photodegradation and water splitting. *Catal Today* 2017; 287(Supplement C):182–8.

[41] Dong F, Wu L, Sun Y, et al. Efficient synthesis of polymeric g-C$_3$N$_4$ layered materials as novel efficient visible light driven photocatalysts. *J Mater Chem* 2011; 21:15171–4.

[42] Kruse N, Chenakin S. XPS characterization of Au/TiO$_2$ catalysts: binding energy assessment and irradiation effects. *Appl Catal A* 2011; 391:367–76.

[43] Chen X, Liu L, Yu PY, et al. Increasing solar absorption for photocatalysis with black hydrogenated titanium dioxide nanocrystals. *Science* 2011; 331:746–50.

[44] da Silva LA, Alves VA, de Castro SC, et al. XPS study of the state of iridium, platinum, titanium and oxygen in thermally formed IrO2+TiO2+PtOX films. *Colloids Surf A* 2000; 170:119–26.

[45] Yang YZ, Chang CH, Idriss H. Photo-catalytic production of hydrogen form ethanol over M/TiO$_2$ catalysts (M = Pd, Pt or Rh). *Appl Catal B* 2006; 67:217–22.

[46] Ou X, Luo Z. One-step synthesis of Ni3S2 nanoplatelets on graphene for high performance supercapacitors. *RSC Adv* 2016; 6:10280–4.

[47] Jian X, Liu X, Yang H-m, et al. Construction of carbon quantum dots/proton-functionalized graphitic carbon nitride nanocomposite via electrostatic self-assembly strategy and its application. *Appl Surf Sci* 2016; 370:514–21.

[48] Yang X, Qian F, Zou G, et al. Facile fabrication of acidified g-C$_3$N$_4$/g-C$_3$N$_4$ hybrids with enhanced photocatalysis performance under visible light irradiation. *Appl Catal B* 2016; 193:22–35.

[49] Ma J, Huang D, Zhang W, et al. Nanocomposite of exfoliated bentonite/g-C$_3$N$_4$/Ag$_3$PO$_4$ for enhanced visible-light photocatalytic decomposition of Rhodamine B. *Chemosphere* 2016; 162:269–76.

[50] Yuan J, Wen J, Zhong Y, et al. Enhanced photocatalytic H2 evolution over noble-metal-free NiS cocatalyst modified CdS nanorods/g-C$_3$N$_4$ heterojunctions. *J Mater Chem A* 2015; 3:18244–55.

[51] Bao Y, Chen K. AgCl/Ag/g-C$_3$N$_4$ hybrid composites: preparation, visible light-driven photocatalytic activity and mechanism. *Nano-Micro Letters* 2016; 8:182–92.

[52] Nong Q, Cui M, Lin H, et al. Fabrication, characterization and photocatalytic activity of g-C$_3$N$_4$ coupled with FeVO$_4$ nanorods. *RSC Adv* 2015; 5:27933–9.

[53] Huang S, Yu Y, Yan Y, et al. Enhanced photocatalytic activity of TiO$_2$ activated by doping Zr and modifying Pd. *RSC Adv* 2016; 6:29950–7.

[54] Wang X, Maeda K, Thomas A, et al. A metal-free polymeric photocatalyst for hydrogen production from water under visible light. *Nat Mater* 2009; 8:76–80.

[55] Djurišić AB, Leung YH, Ching Ng AM. Strategies for improving the efficiency of semiconductor metal oxide photocatalysis. *Mater Horiz* 2014; 1:400–10.

[56] Horikoshi S, Watanabe N, Mukae M, et al. Mechanistic examination of the titania photocatalyzed oxidation of ethanolamines. *New J Chem* 2001; 25:999–1005.

[57] Cultrera A, Boarino L, Amato G, et al. Band-gap states in unfilled mesoporous nc-TiO2: Measurement protocol for electrical characterization. *J Phys D: Appl Phys* 2014; 47:015102.

[58] Zhang J, Ren F, Deng M, et al. Enhanced visible-light photocatalytic activity of a g-C3N4/BiVO4 nanocomposite: a first-principles study. *Phys Chem Chem Phys* 2015; 17:10218–26.

[59] Qiao Q, Yang K, Ma LL, et al. Facile in situ construction of mediator-free direct Z-scheme g-C$_3$N$_4$/CeO$_2$ heterojunctions with highly efficient photocatalytic activity. *J Phys D: Appl Phys* 2018; 51:275302.